Applied Catalysis B: Environmental 130–131 (2013) 187–196

Contents lists available at SciVerse ScienceDirect

Applied Catalysis B: Environmental

journal homepage: www.elsevier.com/locate/apcatb

Tungstophosphoric acid immobilized on ammonium Y and ZSM5 zeolites: Synthesis, characterization and catalytic evaluation

Candelaria Leal Marchena[a,c], Romina A. Frenzel[b,c], Silvina Gomez[a,c], Liliana B. Pierella[a,c,**], Luis R. Pizzio[b,c,*]

[a] Grupo Zeolitas – CITeQ (Centro de Investigación y Tecnología Química), Facultad Regional Córdoba, Universidad Tecnológica Nacional, Maestro Lopez esq Cruz Roja Argentina, 5016 Córdoba, Argentina

[b] Centro de Investigación y Desarrollo en Ciencias Aplicadas "Dr. J.J. Ronco" (CINDECA), Departamento de Química, Facultad de Ciencias Exactas, UNLP-CCT La Plata, CONICET, 47 No. 257, 1900 La Plata, Argentina

[c] Conicet (Consejo Nacional de Investigaciones Científicas y Técnicas), Argentina

ARTICLE INFO

Article history:
Received 6 September 2012
Received in revised form 29 October 2012
Accepted 3 November 2012
Available online 14 November 2012

Keywords:
Tungstophosphoric acid
Zeolites
4-Chlorophenol
Photocatalytic degradation

ABSTRACT

Two series of materials based on tungstophosphoric acid (TPA) immobilized on NH4Y and NH4ZSM5 zeolites were prepared by wet impregnation of the zeolite matrix with TPA aqueous solutions. Their concentration was varied in order to obtain TPA contents of 5, 10, 20 and 30% (w/w) in the solid. The materials were characterized by N_2 adsorption–desorption isotherms, XRD, FT-IR, ^{31}P MAS-NMR, TGA-DSC, DRS–UV–vis, and the acidic behavior was studied by potentiometric titration with n-butylamine.

The specific surface area (S_{BET}) decreased when the TPA content was raised as a result of the zeolite pore blocking. The X-ray diffraction patterns of the solids modified with TPA only presented the characteristic peaks of NH4Y and NH4ZSM5 zeolites, and an additional set of peaks assigned to the presence of $(NH_4)_3PW_{12}O_{40}$. According to the Fourier transform infrared and ^{31}P magic angle spinning-nuclear magnetic resonance spectra, the main species present in the samples (except for NH4YTPA05) is the $[PW_{12}O_{40}]^{3-}$ anion, which was partially transformed into $[P_2W_{21}O_{71}]^{6-}$ anion during the synthesis and drying steps. The thermal stability of the NH4YTPA and NH4ZSM5TPA materials is similar to that of their parent zeolites. Moreover, the samples with the higher TPA content present band gap energy values similar to those reported for TiO_2.

The immobilization of TPA on NH4Y and NH4ZSM5 zeolites is a good method to obtain catalysts with high photocatalytic activity in the 4-chlorophenol degradation. They can be reused at least three times without an important decrease in the degradation degrees.

1. Introduction

The degradation of chemicals present in wastes by heterogeneous photocatalysis is an important issue and its study is a constantly growing field. An increasing number of papers deal with TiO_2 (titania) as one of the most appropriate semiconductor materials to be employed as a photocatalyst, due to its high activity in the photodegradation of organic compounds, low cost, low toxicity, and chemical stability [1–8].

It is generally reported that titania performance in the photodegradation of contaminants contained in wastes is influenced by the crystal structure, crystallinity, surface area, porosity, and band gap energy [9–11], among other factors.

The low surface area and the fast recombination of the photoinduced electrons and holes are the main effects that can lead to a low photocatalytic activity. Transition metals or metal oxides were used as electron trappers to avoid the recombination of the electron–hole pairs of TiO_2-based catalysts [12–15], improving the photocatalytic activity.

Moreover, different heteropolyoxometalates (POM) have been added to titania suspensions [16] or anchored to TiO_2 by chemical interactions [17], incorporated either into titania colloids [18] or into the TiO_2 matrix during the titania gel synthesis [19–21] with the purpose of reducing the charge recombination in UV-illuminated TiO_2. The capacity of heteropolyoxometalates

* Corresponding author at: Centro de Investigación y Desarrollo en Ciencias Aplicadas "Dr. J.J. Ronco" (CINDECA), Departamento de Química, Facultad de Ciencias Exactas, UNLP-CCT La Plata, CONICET, 47 No. 257, 1900 La Plata, Argentina.
Fax: +54 221 425 4477.
** Co-corresponding author at: Grupo Zeolitas – CITeQ (Centro de Investigación y Tecnología Química), Facultad Regional Córdoba, Universidad Tecnológica Nacional, Maestro Lopez esq Cruz Roja Argentina, 5016 Córdoba, Argentina.
E-mail addresses: lpierella@scdt.frc.utn.edu.ar (L.B. Pierella), lrpizzio@quimica.unlp.edu.ar (L.R. Pizzio).

0926-3373/$ – see front matter © 2012 Elsevier B.V. All rights reserved.
http://dx.doi.org/10.1016/j.apcatb.2012.11.002

as acceptors of the electrons of UV-irradiated titania suspensions, generated in the conduction band (e_{cb}^-) together with holes in the valence band (h_{vb}^+), was demonstrated by Park and Choi [22] using a photoelectrochemical method.

POM are widely used as oxidation as well as acid catalysts [23–25]. They are also employed as effective homogeneous photocatalysts in the degradation of organic pollutants in water [26–29].

Heteropolyoxometalates absorb strongly in the near visible and UV region of the light spectrum ($\lambda < 400$ nm). This absorption corresponds to the ligand-to-metal charge-transfer band and it can generate strongly oxidizing excited state POM* (reaction (1)). They are able to carry out the oxidation of organic substrates (S) (reaction (2)) directly via charge transfer or H-atom abstraction, or indirectly through the intermediacy of solvent-derived radicals [29]. After that, the corresponding reduced POM are usually reoxidized to their original oxidation state by an electron acceptor such as dioxygen (reaction (3)).

$$POM + h\nu \rightarrow POM^* \quad (1)$$

$$POM^* + S \rightarrow POM^- + S^+ \quad (2)$$

$$POM^- + O_2 \rightarrow POM + O_2^- \quad (3)$$

The studies on the photocatalytic behavior of POM have been performed mainly on bulk acids and their salts, though, from a practical point of view, supported systems are more interesting. Some of the major drawbacks of POM as catalysts are related to their high solubility in oxygenated solvents and their relatively low specific surface area [23]. Supporting the POM on solids with high surface area is a useful method for improving catalytic performance in liquid–solid and gas–solid heterogeneous reactions. It has been reported that among other factors, the catalytic activity of POM-supported catalyst depends on the support type, the concentration and nature of the chemical species present, and their degree of interaction with the support [20,23]. Silica and NaY zeolite were employed to prepare promising heterogeneous POM-based photocatalysts [30]. According to Ozer and Ferry [30] the use of zeolites as support enhances the "local concentration" of the oxidizable substrate and also the stabilization of charge-transfer state and transient species such as •OH.

Y and ZSM-5 zeolites, with uniform pore size and high specific surface area, are considered as good materials to support and stabilize POM [31–34].

In the present work, we attempted to combine the well-known photocatalytic properties of tungstophosphoric acid, one of the most widely employed POM in homogeneous photocatalysis, and the above-mentioned properties of zeolites as POM supports to synthesize heterogeneous photocatalytic materials.

They were prepared by impregnation of tungstophosphoric acid onto two different zeolites (NH_4Y and NH_4ZSM5) with the aim of studying their influence on the physicochemical and textural characteristics of the solids, and to discuss the effect of the preparation variables on 4-chlorophenol degradation. The photocatalytic degradation of 4-CP has been investigated by many research groups and has become a standard reaction for evaluating various experimental parameters in photocatalysis. To the best of our knowledge, this is the first time that these materials have been successfully synthesized and tested in the photodegradation of this pollutant.

2. Experimental

2.1. Sample preparation

Zeolite NH4Y (Si/Al = 2.47) was provided by Aldrich. ZSM5 material (Si/Al = 17) was obtained by the hydrothermal crystallization method. An aqueous solution of sodium aluminate was added to a silica solution that was previously prepared by partial dissolution of tetrapropylammonium hydroxide (TPAOH) in water. The obtained gel reached a pH > 9 and was maintained at 120–160 °C for 12–16 days under self-generated pressure on autoclave. Afterwards, reaction products were extracted, washed and dried at 110 °C for 12 h. The structure-directing agent (TPAOH) was desorbed in N_2 atmosphere (20 ml/min) at programmed temperature (10 K/min) from 110 to 520 °C and then it was calcined in air at 520 °C for 12 h to obtain Na-HZSM5. The ammonium form of the material (NH4ZSM5) was prepared by ion exchange of NaZSM5 with a NH_4Cl solution (1 M) for 40 h at 80 °C [35].

The tungstophosphoric acid (TPA) solutions were prepared from $H_3PW_{12}O_{40}{\cdot}23H_2O$ (Fluka p.a.) using distilled water as solvent. The incorporation of TPA ($H_3PW_{12}O_{40}$) onto the zeolite matrix was realized by wet impregnation in a rotary evaporator at 80 °C. The amount of TPA to be deposited onto the surface of the zeolite was varied with the purpose of obtaining a TPA concentration of 5%, 10%, 20% and 30% by weight in the final solids that, for zeolite NH4Y, were named NH4YTPA05, NH4YTPA10, NH4YTPA20 and NH4YTPA30, respectively; and for zeolite NH4ZSM5, NH_4ZSM5TPA05, NH_4ZSM5TPA10, NH_4ZSM5TPA20 and NH_4ZSM5TPA30, respectively. The solids were dried under vacuum at 80 °C.

2.2. Sample characterization

2.2.1. Textural properties

The specific surface area and the mean pore diameter of the solids were determined from the N_2 adsorption–desorption isotherms at the liquid-nitrogen temperature, obtained using Micromeritics PulseChemisorb 2700 equipment. The solids were previously degassed at 100 °C for 2 h.

2.2.2. Nuclear magnetic resonance spectroscopy

The ^{31}P magic angle spinning-nuclear magnetic resonance (^{31}P MAS-NMR) spectra were recorded with Bruker Avance II equipment, using the CP/MAS ^1H–^{31}P technique. A sample holder of 4 mm diameter and 10 mm in height was employed, using 5 μs pulses, a repetition time of 4 s, and working at a frequency of 121.496 MHz for ^{31}P at room temperature. The spin rate was 8 kHz and several hundred pulse responses were collected. Phosphoric acid 85% was employed as external reference.

2.2.3. Fourier transform infrared spectroscopy

The Fourier transform infrared FT-IR spectra of the solids were obtained using a JASCO 5300 spectrometer and pellets in KBr in the 400–4000 cm^{-1} wavenumber range.

2.2.4. X-ray diffraction

The X-ray diffraction (XRD) patterns were recorded with Philips PW-3020 equipment with a built-in recorder, using CuKα radiation, nickel filter, 20 mA and 40 kV in the high voltage source, and scanning angle between 5° and 50° 2θ at a scanning rate of 2° per min.

2.2.5. Thermogravimetric analysis and differential scanning calorimetry

The TGA-DSC measurements of the solids were carried out using a Shimadzu DT 50 thermal analyzer. The thermogravimetric and differential scanning calorimetry analyses were performed under argon or nitrogen, respectively, using 20–30 mg samples and a heating rate of 10 °C/min. The studied temperature range was 20–700 °C.

2.2.6. Diffuse reflectance spectroscopy

The diffuse reflectance spectra (DRS) of the materials were recorded using a UV–visible Lambda 35, Perkin Elmer spectrophotometer, to which a diffuse reflectance chamber Labsphere RSA-PE-20 with an integrating sphere of 50 mm diameter and internal Spectralon coating is attached, in the 200–800 nm wavelength range.

2.2.7. Potentiometric titration

The acidity of the solids was estimated by means of potentiometric titration. A known mass of solid was suspended in acetonitrile and stirred for 3 h. Then, the suspension was titrated with 0.05 N n-butylamine in acetonitrile using Metrohm 794 Basic Titrino apparatus with a double junction electrode.

2.3. Photodegradation reaction

The catalytic activity of the materials was evaluated in the photodegradation of 4-chlorophenol (Fluka) in water, at 25 °C. The tests were carried out employing a 125 W high-pressure mercury lamp (with a maximum emission at about 365 nm) placed inside a Pyrex glass jacket, thermostated by water circulation, and immersed in the 4-chlorophenol (4-CP) solution contained in a 300 ml cylindrical Pyrex glass reactor. The catalyst was maintained in suspension by stirring and air was continuously bubbled. Previously, the 4-CP solution (200 ml, 1.5×10^{-4} mol/l) containing 200 mg of catalyst was magnetically stirred in the absence of light for 60 min to ensure that the adsorption–desorption equilibrium of 4-CP on the surface of the materials is attained. During the course of the experiments, samples (3 ml) were periodically withdrawn, filtered using a Millipore syringe adapter (porosity, 0.45 μm) and then analyzed. The variation of the 4-CP concentration as a function of the reaction time was determined by a UV-visible LAMBDA 35 Perkin Elmer double-beam spectrophotometer, measuring the absorbance at 225 nm. The concentration of released chloride ions was measured by a selective Cl^- electrode (pHoenix CLO1508) with an ion meter (Consort P903). The filtrates were extracted three times with ethyl ether, the organic layers were collected, dried with sodium sulfate, and concentrated for the determination of the intermediates using a Hewlett Packard 6890 N GC/MSD. The extent of 4-CP mineralization was determined using the Total Organic Carbon, Method 10129 DR/4000 (HACH).

In order to evaluate the possibility of TPA leaching during the photocatalytic degradation of 4-CP, at the end of each experiment, the catalyst was separated by centrifugation, and W was determined in the liquid phase by atomic absorption spectrometry using a Varian AA Model 240 spectrophotometer. The calibration curve method was used with standards prepared in the laboratory. The analyses were carried out at a wavelength of 254.9 nm, bandwidth 0.3 nm, lamp current 15 mA, phototube amplification 800 V, burner height 4 mm, and acetylene-nitrous oxide flame (11:14).

3. Results and discussion

The specific surface area (S_{BET}) of the synthesized materials, together with the zeolite NH_4Y, NH_4ZSM5 and TPA samples, determined from N_2 adsorption–desorption isotherms using Brunauer–Emmett–Teller (BET) method, is listed in Table 1.

The N_2 adsorption–desorption isotherms of the $NH_4YTPA05$, $NH_4YTPA10$, $NH_4YTPA20$, and $NH_4YTPA30$ samples exhibit similar characteristics to that of NH_4Y zeolite. According to IUPAC classification, they are Type I isotherms, characteristic of microporous solids having relatively small external surfaces. The S_{BET} decreases with the increment of TPA content in the sample.

Table 1
Specific surface area, crystallite size and optical band gap of TPA, NH_4Y, NH_4ZSM5, TPA-zeolites samples.

Samples	S_{BET} (m^2/gr)	D_C[a] (nm)	E_g (eV)
TPA	2	5.0	2.8
NH_4Y	485	1.1	5.10
$NH_4YTPA05$	438	0.9	3.30
$NH_4YTPA10$	408	0.9	3.25
$NH_4YTPA20$	394	0.9	3.22
$NH_4YTPA30$	366	0.9	3.10
NH_4ZSM5	355	0.4	5.70
$NH_4ZSM5TPA05$	337	0.6	3.25
$NH_4ZSM5TPA10$	335	0.6	3.20
$NH_4ZSM5TPA20$	322	0.6	3.18
$NH_4ZSM5TPA30$	323	0.6	3.18

[a] D_C values of TPA, NH_4Y, and NH_4ZSM5 samples were calculated using the (2, 2, 2), (1, 1, 1) and (1, 0, 1) crystal plane respectively.

A similar behavior was observed in the samples obtained by impregnation of the NH_4ZSM5 zeolite, although the decrease in S_{BET} was significantly lower (Table 1).

Taking into account that $[PW_{12}O_{40}]^{3-}$ anions have a diameter of 1.2 nm [36], the progressive decrease of S_{BET} could be due to the clogging of the pores of NH_4Y and NH_4ZSM5 zeolites.

The XRD patterns of the samples NH4YTPA05, NH4YTPA10, NH4YTPA20 and NH4YTPA30 (Fig. 1), and NH4ZSM5TPA05, NH4ZSM5TPA10, NH4ZSM5TPA20 and NH4ZSM5TPA30 show the characteristic peaks of NH4Y and NH4ZSM5 zeolites, respectively. However, their intensity decreases in parallel with the increment of TPA content. The XRD diffraction patterns also present an additional set of peaks, which are different from those characteristic of the tungstophosphoric acid ($H_3PW_{12}O_{40}$), its more common hydrates ($H_3PW_{12}O_{40}{\cdot}23H_2O$ and $H_3PW_{12}O_{40}{\cdot}6H_2O$), or other crystalline phases resulting from their transformation [37]. These peaks are similar to those characteristic of the cubic structure of $(NH_4)_3PW_{12}O_{40}$, whose formation takes place as a result of the interaction between $[PW_{12}O_{40}]^{3-}$ anions and $[NH_4]^+$ cations present in the zeolite matrix.

The crystallite size (D_C) of the new crystalline phase, estimated by XRD using the Scherrer equation, seems to be independent of the TPA content in the prepared materials (NH4YTPA and NH4ZSM5TPA), and it is similar to that of parent zeolite (Table 1).

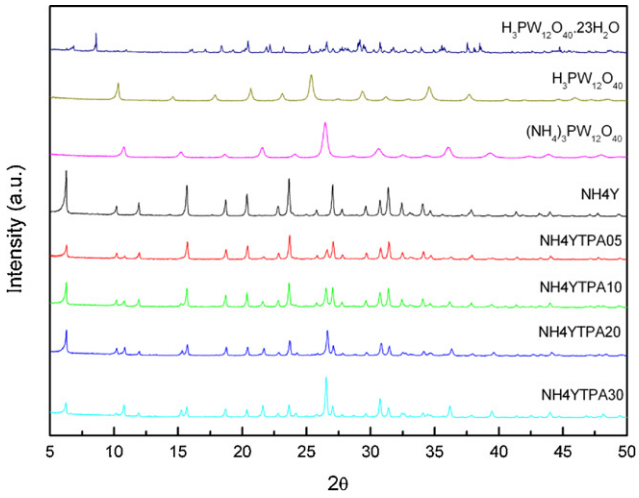

Fig. 1. XRD patterns of $H_3PW_{12}O_{40}{\cdot}23H_2O$ (JCPDS N° 50-0655), $H_3PW_{12}O_{40}$ (JCPDS N° 50-0657), $(NH_4)_3PW_{12}O_{40}$ (JCPDS N° 50-0305), NH4Y(JCPDS N° 73-2311), and the samples obtained by their impregnation with TPA: NH4YTPA05, NH4YTPA10, NH4YTPA20, and NH4YTPA30.

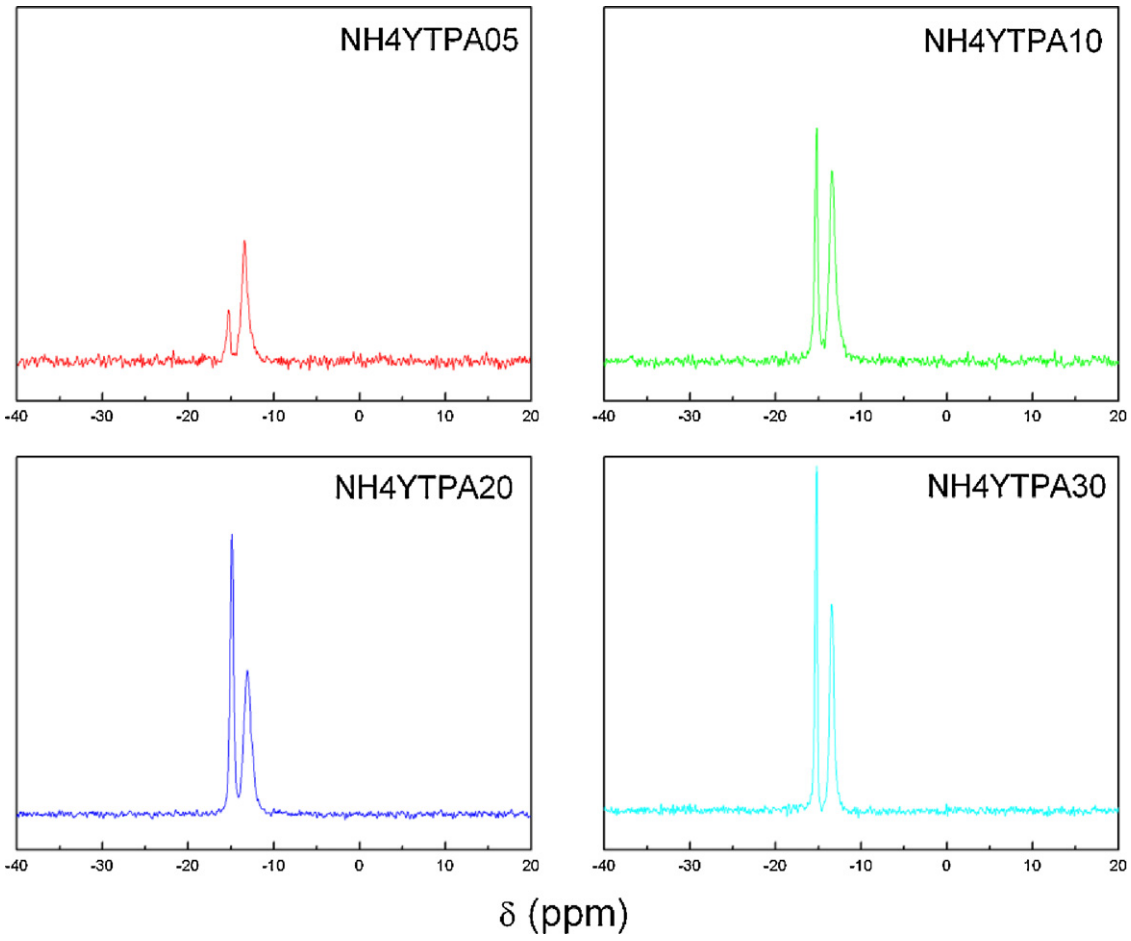

Fig. 2. ^{31}P MAS-NMR spectra of NH4YTPA05, NH4YTPA10, NH4YTPA20, and NH4YTPA30 samples.

The interaction between $H_3PW_{12}O_{40}$ and supports such as SiO_2, TiO_2, or ZrO_2 can be assumed to be of the electrostatic type due to transfer of protons to M—OH according to [38]:

$$M{-}OH + H_3PW_{12}O_{40} \rightarrow [M{-}OH_2^+][H_2PW_{12}O_{40}^-]$$

It has been reported that proton transfer from TPA to the amine group, resulting in an electrostatic bond between $-NH_3^+$ and $[H_{3-x}PW_{12}O_{40}]^{x-}$ (where $1 < x \leq 3$), is responsible for the efficient immobilization of the heteropolyanion [39,40].

The ^{31}P MAS-NMR spectra of NH4YTPA05, NH4YTPA10, NH4YTPA20, and NH4YTPA30 samples (Fig. 2) shows two lines of resonance at −15.2 and −13.4 ppm. These lines can be assigned to the presence of the $[PW_{12}O_{40}]^{3-}$ anion and to the dimeric species $[P_2W_{21}O_{71}]^{6-}$, respectively [41]. We can see that in the spectrum of the sample NH4YTPA05, the line assigned to $[P_2W_{21}O_{71}]^{6-}$ is the most intense. However, the signal at −15.2 ppm is the most important in the rest of the samples. The ratio between the intensity of the signal attributed to the $[PW_{12}O_{40}]^{3-}$ Keggin anion ($I_\delta = -15.2$ ppm) and the one assigned to the dimer $[P_2W_{21}O_{71}]^{6-}$ ($I_\delta = -13.4$ ppm) increases with the increment of TPA content in the material ($I_\delta = -15.2$ ppm/$I_\delta = -13.4$ ppm = 0.42, 1.25, and 1.82 for the NH4YTPA05, NH4YTPA10, and NH4YTPA20 samples respectively) and then remains constant ($I_\delta = -15.2$ ppm/$I_\delta = -13.4$ ppm = 1.78 for the NH4YTPA30 sample).

For the samples NH4ZSM5TPA05, NH4ZSM5TPA10, NH4ZSM5TPA20, and NH4ZSM5TPA30, the ^{31}P MAS-NMR spectra display lines assigned to the Keggin anion and dimeric species attributed to similar values of chemical shift. However, the behavior shown by these samples is slightly different; the signal corresponding to the $[PW_{12}O_{40}]^{3-}$ anion is, in all cases, the most intense. Additionally, the intensity of the signal belonging to the dimer $[P_2W_{21}O_{71}]^{6-}$ decreases and practically disappears when the TPA content increases.

The FT-IR spectrum of TPA (Fig. 3) shows bands at 1081, 982, 888, 793, 595 and 524 cm^{-1}, which are in accordance with those reported in the literature for the $H_3PW_{12}O_{40}$ acid [41]. The first

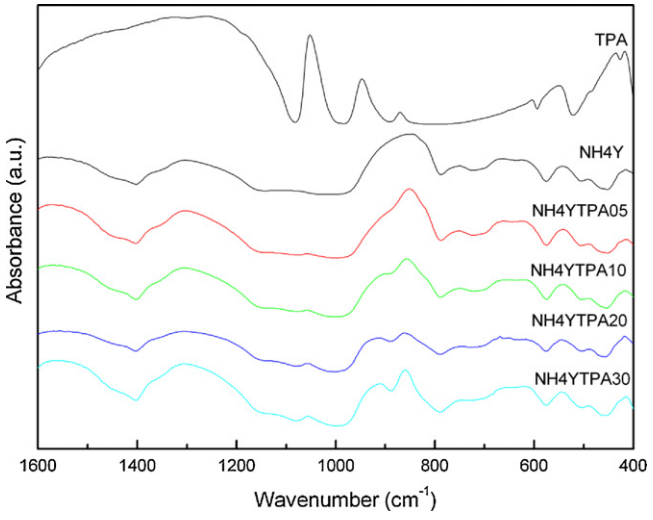

Fig. 3. FT-IR spectra of TPA, NH4Y, NH4YTPA05, NH4YTPA10, NH4YTPA20, and NH4YTPA30 samples.

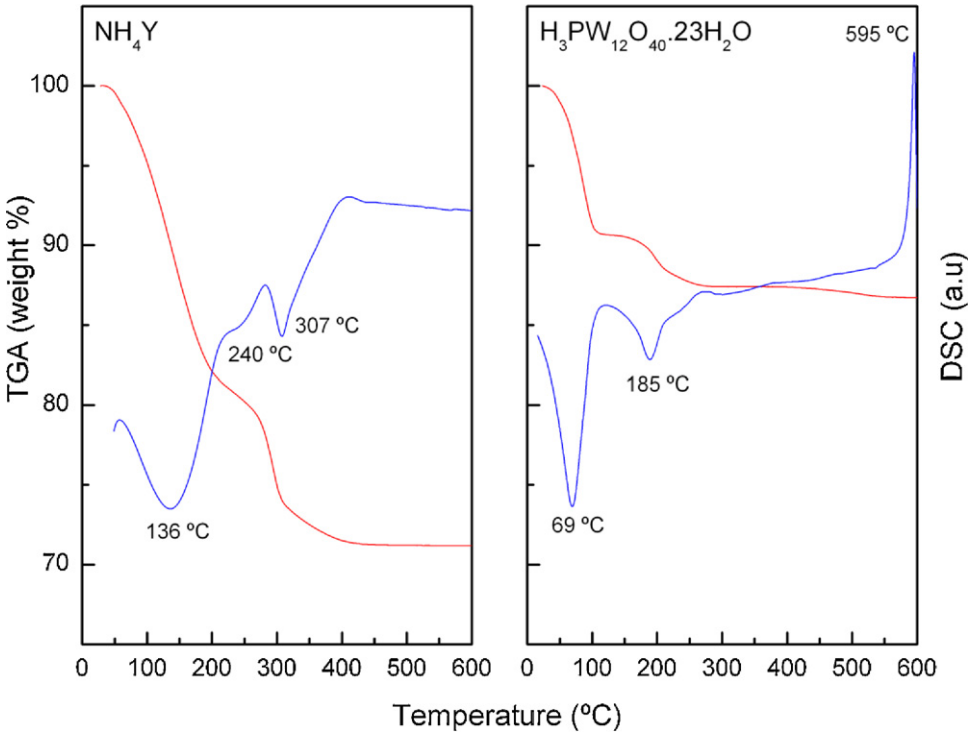

Fig. 4. Thermal analysis diagrams of NH4Y zeolite and $H_3PW_{12}O_{40}{\cdot}23H_2O$ sample.

five bands are assigned to the stretching vibrations P—O_a, W—O_d, W—O_b—W, W—O_c—W, and to the bending vibration O_a—P—O_a, respectively. The subscripts indicate oxygen bridging W and the P heteroatom (a), corner-sharing (b) and edge-sharing (c) oxygen belonging to WO_6 octahedra, and terminal oxygen (d).

In the spectra of the NH4YTPA05, NH4YTPA10, NH4YTPA20, and NH4YTPA30 samples (Fig. 3), overlying the characteristic bands of NH4Y zeolite appears a band at 890 cm^{-1} assigned to the W—O_b—W stretching, whose relative intensity increases with the increment of TPA in the materials. Additionally, a broadening of the zeolite band at 790 cm^{-1} (assigned to the Si—O stretching vibration [42]) takes place as a result of its superposition to the stretching vibration W—O_c—W of TPA.

The main FT-IR bands of the dimer $[P_2W_{21}O_{71}]^{6-}$ assigned to the stretching vibrations P—O, W—O, W—O—W appear at wavenumber values similar to those characteristic of the $[PW_{12}O_{40}]^{3-}$ anion [43]. Taking into account this fact and ^{31}P MAS-NMR results, we can assume that the bands at 890 and 790 cm^{-1} are due to the presence of both $[PW_{12}O_{40}]^{3-}$ and $[P_2W_{21}O_{71}]^{6-}$ species.

For NH4ZSM5TPA05, NH4ZSM5TPA10, NH4ZSM5TPA20 and NH4ZSM5TPA30 samples, the FT-IR spectra present the bands assigned to the W—O_d, W—O_b—W, and W—O_c—W stretching vibrations of $[PW_{12}O_{40}]^{3-}$ anion overlapped to those of the NH4ZSM5. As in the case of NH4YTPA samples, the W—O_c—W vibration produces the broadening of the zeolite band at 800 cm^{-1} assigned to the Si—O stretching vibration.

According to ^{31}P MAS-NMR and FT-IR results, the main species present in the samples (except for NH4YTPA05) is the $[PW_{12}O_{40}]^{3-}$ anion, which was partially transformed into the $[P_2W_{21}O_{71}]^{6-}$ anion during the synthesis and drying steps. This transformation is due to the limited stability range of the $[PW_{12}O_{40}]^{3-}$ anion in solution, which can be increased by adding an organic solvent such as ethanol [44]. At pH 1.5–2, it is reversibly and quickly transformed into the lacunar species $[PW_{11}O_{39}]^{7-}$. Pope [45] has proposed that the following transformation scheme: $[PW_{12}O_{40}]^{3-} \Leftrightarrow [P_2W_{21}O_{71}]^{6-} \Leftrightarrow [PW_{11}O_{39}]^{7-}$ takes place when the pH is increased. This may be considered as a valid path followed by the TPA species during the synthesis of the samples.

The largest proportion of the Keggin anion $[PW_{12}O_{40}]^{3-}$, found in the material obtained by using NH4ZSM5 as support, can be attributed to its higher acidity compared to NH4Y, which limits the transformation of $[PW_{12}O_{40}]^{3-}$ into $[P_2W_{21}O_{71}]^{6-}$.

The DSC diagram of NH4Y zeolite (Fig. 4) exhibits an endothermic peak at 136 °C with a shoulder at 240 °C, and another at 306 °C, due to the desorption of physically adsorbed water, the decomposition of ammonium ions and structural changes, respectively. They are in agreement with those reported in the literature [46]

According to the TGA pattern, the weight loss (25% of the initial mass) associated with the elimination of water and ammonia takes place in two main steps below 300 °C. The weight loss ascribed to the structural changes (dehydroxylation) is rather low (approximately 3%).

The DSC results of $H_3PW_{12}O_{40}{\cdot}21H_2O$ showed two endothermic peaks with maximum at 69 and 185 °C, and an exothermic one with maximum at 595 °C. The endothermic features may be ascribed to the release of physisorbed water and to the dehydration of $H_3PW_{12}O_{40}{\cdot}6H_2O$ phase, respectively, as in the two weight losses below 250 °C observed in the TGA diagram. The exothermic peak may be assigned to the Keggin anion decomposition, which takes place without appreciable weight loss. Another weight loss, equivalent to 1.5 H_2O per Keggin unit, was observed in the TG diagram between 250 and 480 °C. It was assigned to evolution of constitutional water as a result of deprotonation of the heteropolyacid, as it fits well with the loss of the three protons of $H_3PW_{12}O_{40}$ [23,47].

During the water loss processes, Keggin anions are not too much disturbed and near 600 °C they are decomposed into the constituent oxides or, according to Mioc et al. [37], transformed into a new monophosphate bronze type compound PW_8O_{26}.

Fig. 5 shows the DSC diagrams of the samples NH4YTPA05, NH4YTPA10, NH4YTPA20, and NH4YTPA30. They display the characteristic endothermic peaks of NH4Y, although shifted to slightly lower temperatures with increasing TPA content in the sample.

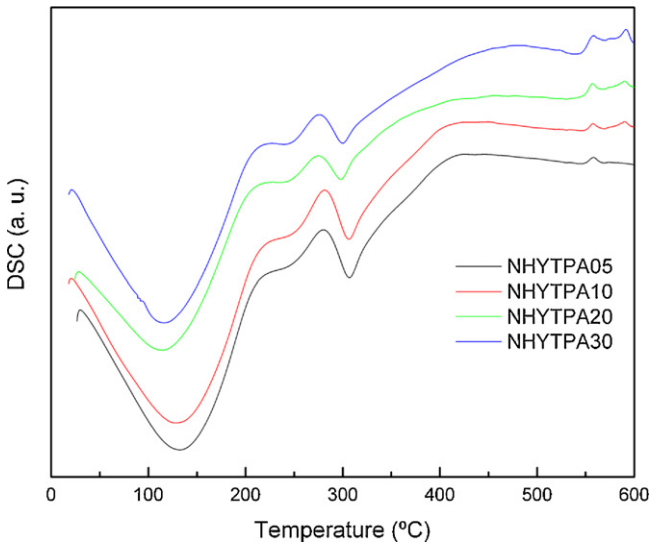

Fig. 5. DSC profiles of the NH_4YTPA05, NH_4YTPA10, NH_4YTPA20, and NH_4YTPA30 samples.

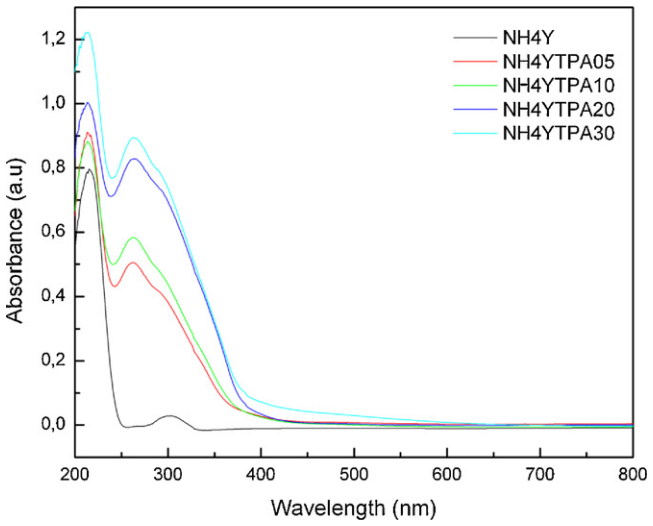

Fig. 6. UV–Vis–DRS spectra of the samples NH4Y, NH4YTPA05, NH4YTPA10, NH4YTPA20, and NH4YTPA30.

The DSC diagram of the samples NH4YTPA10, NH4YTPA20, and NH4YTPA30 shows two exothermic peaks at 558 and 591 °C, which are assigned to the decomposition of the anions $[P_2W_{21}O_{71}]^{6-}$ and $[PW_{12}O_{40}]^{3-}$ [23,48] respectively. In the case of the sample with a lower TPA content, only the peak assigned to the partial decomposition of the dimeric species is present.

The DSC diagram of zeolite NH4ZSM5 presents similar characteristics to that of NH4Y, an endothermic peak at 45 °C with a shoulder peak at 228 °C, and a second one at 377 °C. They are associated with the elimination of physisorbed water, NH_3 and zeolite structural changes, respectively. According to the TGA diagram, the weight loss associated with the release of physisorbed water and ammonia (6% of the initial mass) is considerably lower than that recorded for zeolite NH4Y, and in agreement with the results reported by Decolatti et al. [49]. The weight loss ascribed to structural changes (dehydroxylation) is, in this case, less than 1%.

On the other hand, the DSC diagram of the NH4ZSM5TPA05, NH4ZSM5TPA10, NH4ZSM5TPA20, and NH4ZSM5TPA30 samples presents the endothermic peaks and the shoulder assigned to the elimination of physisorbed water and ammonia, which are in the same temperature range indicated above for the NH4ZSM5 zeolite matrix. However, the peak assigned to structural changes appears displaced to temperatures in the range 400–420 °C in samples with TPA content higher than 5%.

In addition to the above-mentioned peaks, the diagrams show an exothermic peak with maximum at 582 °C assigned to the decomposition of the Keggin anion $[PW_{12}O_{40}]^{3-}$, whose intensity decreases in parallel with the decrease of TPA content in the samples. The absence of the exothermic peak assigned to the $[P_2W_{21}O_{71}]^{6-}$ in this set of samples is due, in accordance with ^{31}P MAS-NMR, to the low amount of the dimer present in the solids.

The charge-transfer absorption spectra of most nonreduced heteropolyanions obtained by UV–Vis–DRS appear in the 200–500 nm region and consist of bands that may be ascribed to oxygen-to-metal transfers. The bulk TPA spectrum presents a band at 212 nm and another broad band that extends from 250 to 450 nm [25,50] assigned to the charge transfer from bridging or terminal O 2p to W 5d (W—O—W and W—O_d, respectively).The UV–Vis–DRS spectra of the samples NH4YTPA05, NH4YTPA10, NH4YTPA20 and NH4YTPA30, together with the zeolite NH4Y, are shown in Fig. 6. The UV–Vis–DRS spectrum of NH4Y presents two bands at 216 and 300 nm assigned to the first one that arose from the Al—O charge-transfer transition of four-coordinated framework aluminum, the second one being attributed to structures with highly ordered octahedral symmetry [51,52].

The addition of TPA leads to an increase in the intensity of the band placed at shorter wavelengths and the appearance of a new one at 263 nm with a shoulder at about 290 nm, which agrees with the values reported by Fox et al. [53] for ammonium salts of the Keggin anion and the dimeric species, respectively.

The UV–Vis–DRS spectra of the samples display an absorption threshold onset that continuously shifts to the visible region with the increment of TPA content. The red shift of the absorption threshold onset is more significant for the NH4YTPA20 and NH4YTPA30 samples.

In the case of the NH4ZSM5TPA05, NH4ZSM5TPA10, NH4ZSM5TPA20, and NH4ZSM5TPA30 samples, the UV–Vis–DRS spectra show only the bands assigned to the ammonium salts of the $[PW_{12}O_{40}]^{3-}$ anion shifted to lower wavelength values (200 and 267 nm, respectively). In comparison to the NH_4Y-based samples, the red shift of the absorption threshold onset of the NH4ZSM5-based ones is small.

The band gap energy values (E_g), estimated from UV–Vis–DRS spectra using Kubelka–Munk remission function [54], are listed in Table 1. These values are similar to those reported in the literature for TiO_2 samples [55].

The E_g values of NH4Y and NH4ZSM5 zeolites without TPA are in agreement with those reported in the literature [56].

The band gap energy values of the samples obtained by impregnation of NH4Y and NH4ZSM5 zeolites with TPA are significantly lower than those of the parent ones. The E_g values decrease slightly with the increment of the TPA content for the NH4YTPA05, NH4YTPA10, NH4YTPA20, and NH4YTPA30 samples. However, they remain practically constant for the NH4ZSM5TPA05, NH4ZSM5TPA10, NH4ZSM5TPA20 and NH4ZSM5TPA30 samples.

Potentiometric titration with n-butylamine let us estimate the number of acid sites and their acid strength. It was suggested that the initial electrode potential (E_i) indicates the maximum acid strength of the sites and the value of meq amine/g solid where the plateau is reached indicates the total number of acid sites. The acid strength of these sites may be classified according to the following scale: $E_i > 100$ mV (very strong sites), $0 < E_i < 100$ mV (strong sites), $-100 < E_i < 0$ (weak sites) and $E_i < -100$ mV (very weak sites) [57].

The titration curves obtained for the samples NH4YTPA05, NH4YTPA10, NH4YTPA20, and NH4YTPA30 are shown in Fig. 7.

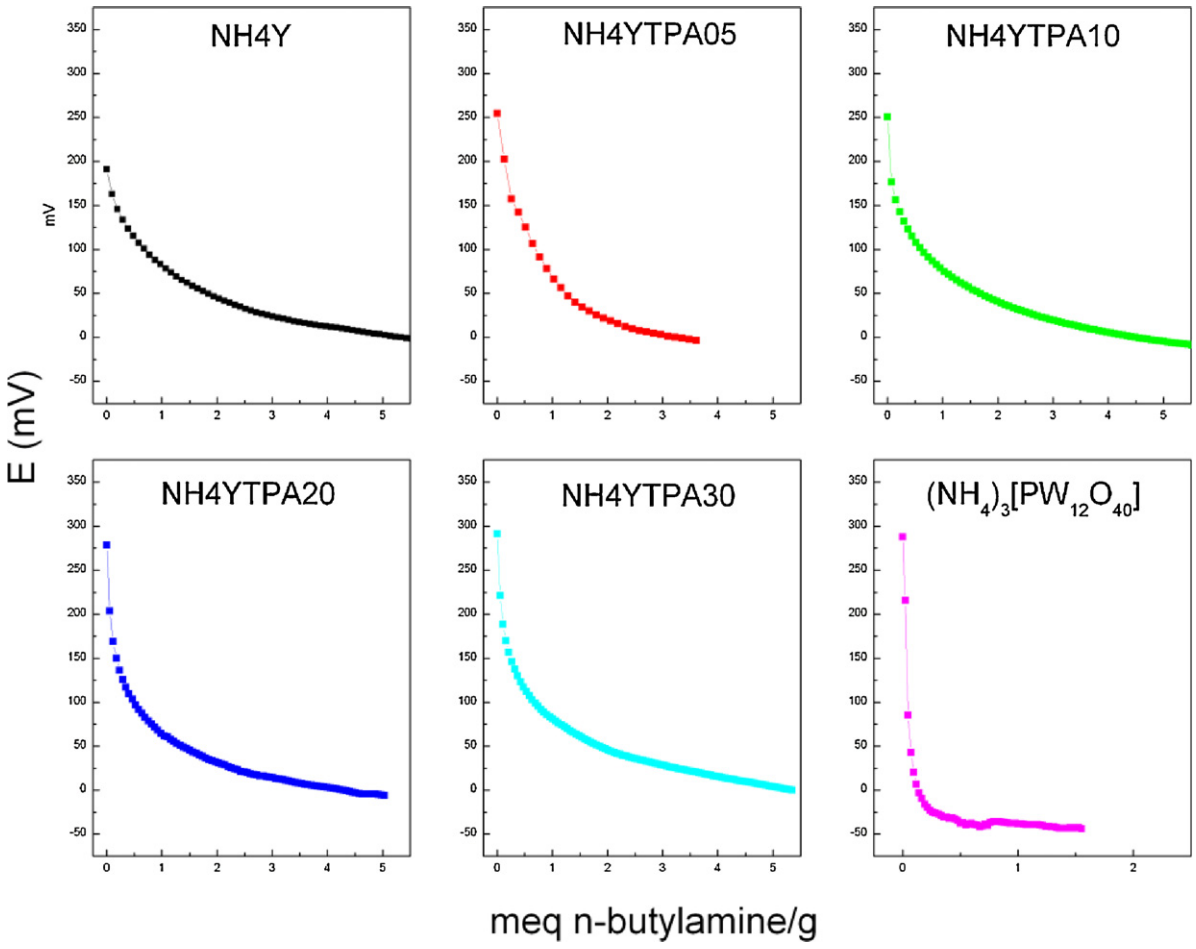

Fig. 7. Potentiometric titration curves of the NH4YTPA05, NH4YTPA10, NH4YTPA20 and NH4YTPA30 samples, and $(NH_4)_3[PW_{12}O_{40}]$.

According to the aforementioned classification, the materials present very strong and strong acid sites, with E_i values in the range 220–290 mV. The E_i value increases with the increment of the TPA content according to the following order: NH4Y (E_i = 190 mV) < NH4YTPA05 (E_i = 224 mV) < NH4YTPA10 (E_i = 251 mV) < NH4YTPA20 (E_i = 278 mV) < NH4YTPA30 (E_i = 291 mV).

Additionally, the E_i values of the samples with higher TPA content are close to that of the salt $(NH_4)_3PW_{12}O_{40}$ (E_i = 288 mV), which is significantly lower than the value reported for $H_3PW_{12}O_{40}{\cdot}21H_2O$ (E_i = 538 mV) or its partially substituted Cs or K salts [58]. Moreover, the amount of acid sites determined by this technique is practically independent of the TPA content and it is similar to that of NH4Y zeolite.

On the other hand, as above-mentioned, NH4Y presents lower acidity than NH4ZSM5 (E_i = 251 mV) and the acidity of the NH4ZSM5TPA samples also increases with the increment of TPA content following the order: NH4ZSM5 (E_i = 251 mV) < NH4ZSM5TPA05 (E_i = 254 mV) < NH4ZSM5TPA10 (E_i = 266 mV) < NH4ZSM5TPA20 (E_i = 282 mV) < NH4ZSM5TPA30 (E_i = 294 mV). Additionally, the amount of acid sites was determined to be independent of the TPA content and similar to that of the unmodified zeolite.

In summary, the acid properties of both series of TPA-modified zeolites are rather similar, despite the higher acid strength of NH4ZSM5.

The synthesized materials were tested in the photocatalytic degradation of 4-chlorophenol (4-CP) at the pH of the suspension obtained by the addition of 100 mg of catalyst to 200 ml of a 4-CP water solution (1.5×10^{-4} mol/l). The initial and the final pH of the solutions were in the range 6.5–5.0. The 4-CP (a weak acid of pKa = 9.41) under these experimental conditions was mainly present in the nonionized form, and the surface of the catalysts was mostly negatively charged. Therefore, the adsorption of 4-CP on the catalyst surface does not take place in a detectable degree.

The amount of 4-CP degraded after 360 min of irradiation but without catalyst was only of 6%, and it is mainly due to a photolytic process [59]. The 4-CP degradation was not detected under the same experimental conditions but with the mercury lamp turned off.

The diminution of the 4-CP concentration was only 8% for the NH4Y sample at 360 min under reaction and it was similar to that achieved without catalyst. However, for the TPA-modified samples, the 4-CP degradation at the same time is significantly higher, and the 4-CP concentration decline (depletion) increases in parallel with the increment of TPA in the samples NH4YTPA05 < NH4YTPA10 < NH4YTPA20 < NH4YTPA30. From the comparison of the 4-CP degradation profiles (Fig. 8a), we can see that the 4-CP degradation rates increase when the TPA content is raised, though the increase is lower when the TPA amount changes from 20% to 30%.

The catalytic activity of the bulk $(NH_4)_3[PW_{12}O_{40}]$ salt was measured under the same experimental conditions to be compared with those of the synthesized materials. In this test, the amount of $(NH_4)_3[PW_{12}O_{40}]$ was fixed in order obtain a TPA amount similar to that contained in the NH4YTPA30 sample. The 4-CP concentration decreased by 28% at 360 min under reaction and it was lower than those obtained using the NH4YTPA30 samples (82%). The rather

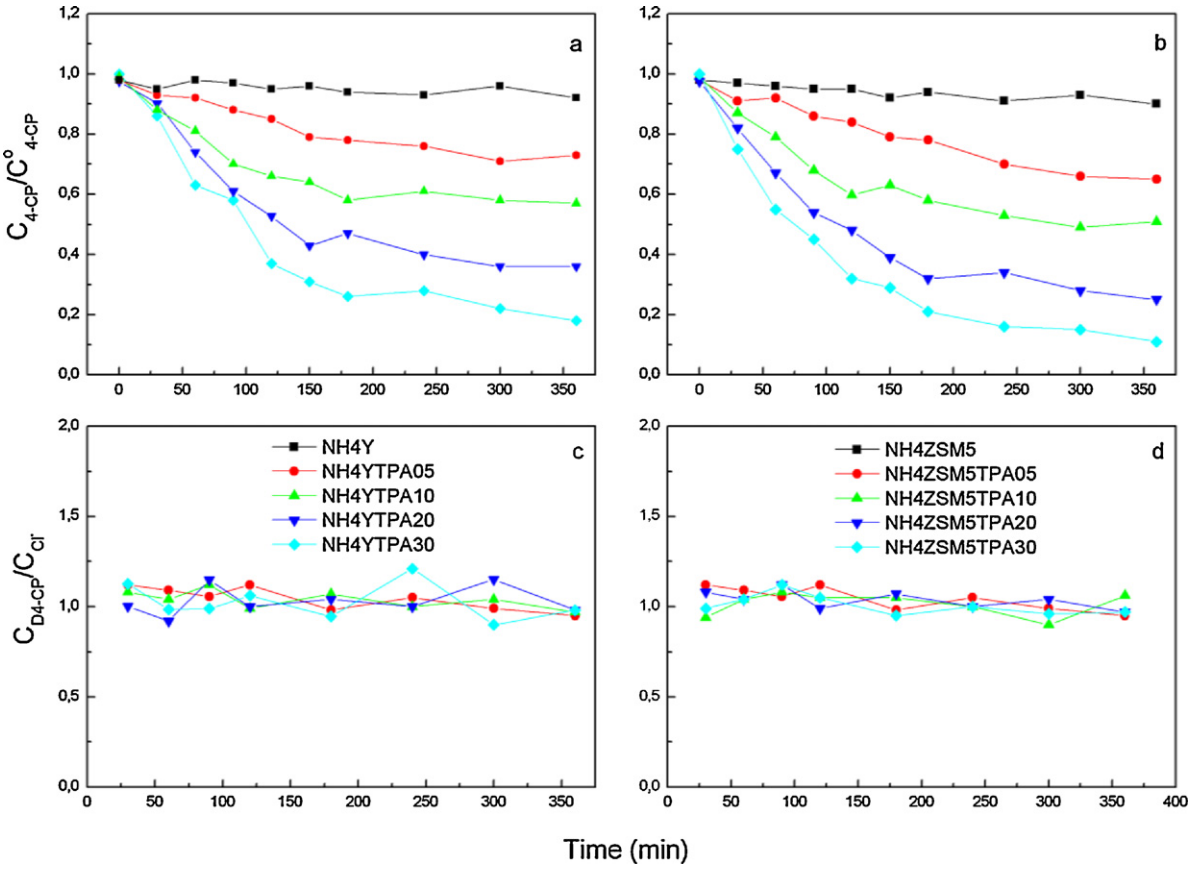

Fig. 8. Photocatalytic degradation of 4-CP and ratio between the amount of degraded 4-CP and the amount of released chloride ions as a function of the irradiation time for the NH4YTPA and NH4ZSM5TPA samples.

poor catalytic behavior of the $(NH_4)_3[PW_{12}O_{40}]$ salt could be due to lower specific surface area of ammonium salt (125 m^2/g).

The 4-CP degradation profiles using NH4ZSM5TPA samples (Fig. 8b) are very similar to those of the NH4YTPA materials, and they show that 4-CP degradation rates increase when the TPA content is raised. Also in this case the increment of the degradation rate is lower when the TPA content is raised from 20% to 30%.

On the other hand, regardless of the TPA content employed, the 4-CP degradation achieved at any time was slightly higher when NH4ZSM5TPA materials were used as catalyst.

The increment of the catalytic activity when the TPA content increases is principally due to the direct participation of TPA in the degradation of the organic substrate (reactions (1)–(3)) and/or in the production of the •OH reactive species (reaction (4)) that participates in the degradation of the organic substrate (reaction (5)) [60].

$$POM^{*} + H_2O \rightarrow POM^{-} + {}^{\bullet}OH + H^{+} \quad (4)$$

$$^{\bullet}OH + S \rightarrow \text{oxidationproducts} \quad (5)$$

Additionally, the increment of the catalytic activity can also be due to the lower *band gap* values of the samples with higher TPA contents, which would increase the absorption capacity of higher wavelength radiation.

Taking into account that the E_g values of NH4ZSM5TPA and NH4YTPA with the same TPA content are similar, the higher catalytic activity of the former could be assigned to the largest proportion of the $[PW_{12}O_{40}]^{3-}$ anion present as a new crystalline phase with lower D_p in the materials obtained using NH4ZSM5 as support, as was revealed by ^{31}P MAS-NMR and XRD, respectively.

The ratio between the amount of degraded 4-CP ($C_{D4C\text{-}P}$) and the amount of released chloride ions (C_{Cl^-}) as a function of the irradiation time during the 4-CP photodegradation catalyzed by NH4YTPA and NH4ZSM5TPA samples are shown in Fig. 8c and d, respectively. It can be observed that the $(C_{D4C\text{-}P})/(C_{Cl})$ ratio remains practically equal to the unit during the course of the photodegradation. These results are in agreement with previous reports that indicate that the cleavage of the Cl-aryl bond, releasing inorganic chloride to the reacting medium, is the first step during the photocatalytic degradation of 4-CP. Benzoquinone (BQ), hydroquinone (HQ) and 4-chlorocatechol (4-CC) have been reported as the main aromatic reaction intermediates during the photodegradation of 4-CP [61–63].

Benzoquinone and hydroquinone were reported as the major intermediaries when 4-CP was photodegraded using polyoxometalates [26] and silica-immobilized polyoxometalates [64]. We found that, in our experimental conditions, BQ was the predominant intermediate and HQ was present as traces.

To evaluate the reusability of the catalysts we chose NH4YTPA30 and NH4ZSM5TPA30. To this end, after each photocatalytic experiment, the catalysts were separated from the resulting suspension by centrifugation, washed with distilled water, dried at 70 °C and reused.

The percentage of degraded 4-CP after each cycle of usage, together with the mineralization degree, is shown in Fig. 9. The latter was slightly lower than the amount of degraded 4-CP as a result of the formation of organic intermediates previously mentioned. The results indicate that both decrease slightly during the first reuse, and then keep constant. The decrease was assigned to the solubilization of TPA (less than 3% of the TPA content) from the fresh samples during the first and the second catalytic tests, as

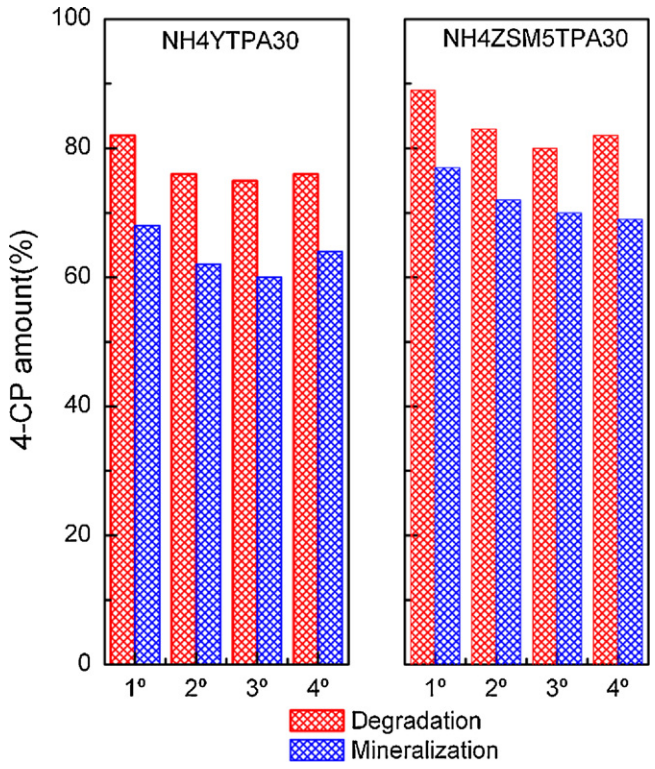

Fig. 9. 4-CP degradation and mineralization degree as a function of the number cycle of usage for the NH4YTPA30 and NH4ZSM5 samples.

was established by atomic absorption spectrometry. Finally, these results show that after the third use the catalytic performance of the selected samples is the same, and the synthesized materials can be considered as suitable photocatalysts to degrade a toxic chlorinated phenol.

4. Conclusions

Materials based on tungstophosphoric acid immobilized over NH_4Y and NH_4ZSM5 zeolites were prepared by wet impregnation.

FT-IR and ^{31}P MAS-NMR results indicated that the main species present in the samples (except for NH4YTPA05) is the $[PW_{12}O_{40}]^{3-}$ anion, which was partially transformed into $[P_2W_{21}O_{71}]^{6-}$ anion during the synthesis and drying steps. In the case of the NH4ZSM5-based samples, the transformation of $[PW_{12}O_{40}]^{3-}$ into $[P_2W_{21}O_{71}]^{6-}$ took place in lower proportion.

The specific surface area of the samples decreased with the increase of the TPA content as a result of the zeolite pore blocking, attributed to clogging of zeolite pores by the $[PW_{12}O_{40}]^{3-}$ and $[P_2W_{21}O_{71}]^{6-}$ species.

According to DSC and TGA results, the thermal stability of the NH_4YTPA and $NH_4ZSM5TPA$ materials is similar to that of their parent zeolites. Moreover, the decomposition of the anions $[PW_{12}O_{40}]^{3-}$ and $[P_2W_{21}O_{71}]^{6-}$ takes place at temperatures similar to those reported for the bulk compounds.

The DRS results indicate that the addition of TPA generates a red shift of the absorption threshold onset, which is more significant for the samples with the higher TPA content and whose band gap energy values are similar to those reported for TiO_2.

According to the results presented in this work, the materials obtained by impregnation of TPA onto the zeolite matrix, NH4Y and NH4ZSM5, present suitable textural and physicochemical properties to be used as catalysts in the photocatalytic treatment of wastewater that contains chlorinated phenols.

Acknowledgements

The authors thank Dra. D. Lick, G. Valle and L. Osiglio for their experimental contribution and to CONICET and UNLP for the financial support.

Appendix A. Supplementary data

Supplementary data associated with this article can be found, in the online version, at http://dx.doi.org/10.1016/j.apcatb.2012.11.002.

References

[1] J.M. Herrann, Applied Catalysis B: Environmental 99 (2010) 461.
[2] A. Sclafani, L. Palmisano, E. Davì, Journal of Photochemistry and Photobiology A: Chemistry 56 (1991) 113.
[3] D.M. Antonelli, Y.J. Ying, Angewandte Chemie (International Ed. In English) 34 (1995) 2014.
[4] S. Sakthivel, M.V. Shankar, M. Palanichamy, B. Arabindoo, D.W. Bahnemann, V. Murugesan, Water Research 38 (2004) 3001.
[5] K.L. Yeung, S.T. Yau, A.J. Maira, J.M. Coronado, J. Soria, P.L. Yue, Journal of Catalysis 219 (2003) 107.
[6] J.C. Yu, J. Lin, D. Lo, S.K. Lam, Langmuir 16 (2000) 7304.
[7] K.-H. Wang, H.-H. Tsai, Y.-H. Hsieh, Applied Catalysis B: Environmental 17 (1998) 313.
[8] R. Van Grieken, J. Aguado, M.J. López-Muñoz, J. Marugán, Journal of Photochemistry and Photobiology A: Chemistry 3010 (2002) 1.
[9] X. Li, J.W. Cubbage, T.A. Tetzlaff, W.S. Jenks, Journal of Organic Chemistry 64 (1999) 8509–8524.
[10] K.B. Kyoko, S. Kazuhiro, K. Hitoshi, O. Kiyomi, A. Hironori, Applied Catalysis A-General 165 (1997) 394.
[11] S. Sakulkhaemaruethai, S. Pavasupree, Y. Suzuki, S. Yoshikawa, Materials Letters 59 (2005) 2965.
[12] W. Lee, Y.M. Gao, K. Dwight, A. Wold, Materials Research Bulletin 27 (1992) 685.
[13] A. Sclafani, M.N. Mozzanega, P. Pichat, Journal of Photochemistry and Photobiology A: Chemistry 59 (1991) 181.
[14] W. Lee, Y.R. Do, K. Dwight, A. Wold, Materials Research Bulletin 28 (1993) 1127.
[15] S. Ikeda, N. Sugiyama, B. Pal, G. Marci, L. Palmisano, H. Noguchi, K. Uosaki, B. Ohtani, Physical Chemistry Chemical Physics 3 (2001) 267.
[16] R.R. Ozer, J.L. Ferry, Environmental Science and Technology 35 (2001) 3242.
[17] Y. Yang, Y. Guo, C. Hu, Y. Wang, E. Wang, Applied Catalysis A-General 273 (2004) 201.
[18] M. Yoon, J.A. Chang, Y. Kim, J.R. Choi, K. Kim, S.J. Lee, Journal of Physical Chemistry B 105 (2001) 2539.
[19] V.M. Fuchs, E.L. Soto, M.N. Blanco, L.R. Pizzio, Journal of Colloid and Interface Science 327 (2008) 403.
[20] M.N. Blanco, L.R. Pizzio, Applied Surface Science 256 (2010) 3546.
[21] V.M. Fuchs, L. Méndez, M.N. Blanco, L.R. Pizzio, Applied Catalysis A-General 358 (2009) 73.
[22] H. Park, W. Choi, Journal of Physical Chemistry B 107 (2003) 3885.
[23] T. Okuhara, N. Mizuno, M. Misono, Advances in Catalysis 41 (1996) 221.
[24] V.M. Fuchs, L.R. Pizzio, M.N. Blanco, Catalysis Today 133–135 (2008) 181.
[25] L.R. Pizzio, C.V. Cáceres, M.N. Blanco, Applied Catalysis A-General 167 (1998) 283.
[26] A. Mylonas, A. Hiskia, E. Papaconstantinou, Journal of Molecular Catalysis A: Chemical 114 (1996) 191.
[27] A. Mylonas, E. Papaconstantinou, Journal of Photochemistry and Photobiology 94 (1996) 77.
[28] C. Hu, B. Yue, T. Yamase, Applied Catalysis A-General 194–195 (2000) 99.
[29] R.R. Ozer, J.L. Ferry, Journal of Physical Chemistry B 104 (2000) 9444.
[30] R.R. Ozer, J.L. Ferry, Journal of Physical Chemistry B 106 (2002) 4336.
[31] S. Anandan, S.Y. Ryu, W.J. Cho, M. Yoon, Journal of Molecular Catalysis A: Chemical 195 (2003) 201.
[32] M.I. Ahmad, S.M.J. Zaidi, S.U. Rahman, S. Ahmed, Microporous and Mesoporous Materials 91 (2006) 296.
[33] S.R. Mukai, L. Lin, T. Masuda, K. Hashimoto, Chemical Engineering Science 56 (2001) 799.
[34] K. Pamin, A. Kubacka, Z. Olejniczak, J. Haber, B. Sulikowski, Applied Catalysis A 194 (2000) 137.
[35] Occluded cobalt species over ZSM-5 matrix: Design, preparation, characterization and magnetic behavior, 29, L.B. Pierella, Doctoral Thesis, Universidad Nacional de Córdoba, 2000.
[36] Y. Izumi, K. Matsuo, K. Urabe, Journal of Molecular Catalysis 18 (1983) 299.
[37] J.B. Mioc, R.Z. Dimitrijevi, M. Davidovic, Z.P. Nedic, M.M. Mitrovic, P.H. Colomban, Journal of Materials Science 29 (1994) 3705.
[38] F. Lefebvre, Journal of the Chemical Society, Chemical Communications (1992) 756.
[39] L. Pizzio, P. Vázquez, A. Kikot, E. Basaldella, C. Cáceres, M. Blanco, Studies in Surface Science and Catalysis 143 (2002) 739.

[40] M. Hasik, W. Turek, E. Stochmal, M. Lapkowski, A. Pron, Journal of Catalysis 147 (1994) 544.
[41] R. Massart, R. Contant, J. Fruchart, J. Ciabrini, M. Fournier, Inorganic Chemistry 16n (1977) 2916;
C. Rocchiccioli-Deltcheff, R. Thouvenot, R. Franck, Spectrochimica Acta 32A (1976) 587.
[42] I. Othman, R.M. Mohamed, I.A. Ibrahim, Applied Catalysis A-General 299 (2006) 95.
[43] R. Contant, Canadian Journal of Chemistry 65 (1987) 568.
[44] I.V. Kozhevnikov, Chemical Reviews 98 (1998) 171–198.
[45] M.T. Pope, Heteropoly and Isopoly Oxometalates, Springer-Verlag, Heidelberg, 1983, p. 58.
[46] F. Su, X.S. Zhao, L. Lv, Z. Zhou, Carbon 42 (2004) 2821.
[47] M. Fournier, C. Feumi-Jantou, C. Rabia, G. Hervé, S. Launary, Journal of Materials Chemistry 2 (1992) 971.
[48] A.V. Ivanov, T.V. Vasina, V.D. Nissenbaum, L.M. Kustov, M.N. Timfeeva, J.I. Houzvicka, Applied Catalysis A 259 (2004) 65.
[49] H.P. Decolatti, A. Martínez-Hernández, L.B. Gutiérrez, G.A. Fuentes, J.M. Zamaro, Microporous and Mesoporous Materials 145 (2011) 41.
[50] P. Vázquez, L. Pizzio, C. Cáceres, M. Blanco, H. Thomas, E. Alesso, L. Finkielsztein, B. Lantaño, G. Moltrasio, J. Aguirre, Journal of Molecular Catalysis A: Chemical 161 (2000) 223.
[51] E.D. Garbowski, C. Mirodatos, Journal of Physical Chemistry 86 (1982) 97–102.
[52] M.A. Zanjanchi, A. Razavi, Spectrochimica Acta, Part A 57 (2001) 119.
[53] M.A. Fox, R. Cardona, E. Gaillard, Journal of the American Chemical Society 109 (1987) 6347.
[54] S.P. Tandom, J.P. Gupta, Physica Status Solidi 38 (1970) 363.
[55] E. Joselevich, I. Willner, Journal of Physical Chemistry 98 (1994) 7628.
[56] G. Yan, J. Long, X. Wang, Z. Li, X. Fu, Comptes Rendus Chimie 11 (2008) 114.
[57] R. Cid, G. Pecci, Applied Catalysis A-General 14 (1985) 15.
[58] L.R. Pizzio, M.N. Blanco, Applied Catalysis A-General 255 (2003) 265.
[59] M.A. Barakat, H. Schaeffer, G. Hayes, S. Ismat-Shah, Applied Catalysis B: Environmental 57 (2005) 23.
[60] S. Antonaraki, T.M. Triantis, E. Papaconstantinou, A. Hiskia, Catalysis Today 151 (2010) 119.
[61] M.G. Kang, H.E. Han, K.J. Kim, Journal of Photochemistry and Photobiology A: Chemistry 125 (1999) 119.
[62] H.H. Oua, S.L. Loa, C.H. Wu, Journal of Hazardous Materials B 137 (2006) 1362.
[63] N. Venkatachalam, M. Palanichamy, B. Arabindoo, V. Murugesan, Journal of Molecular Catalysis A: Chemical 266 (2007) 158.
[64] B. Yue, Y. Zhou, J. Yuxu, Z. Wu, X. Zhang, Y. Zou, S. Jin, Environmental Science and Technology 36 (2002) 1325.